PERGAMON

Atmospheric Environment 34 (2000) 4155–4173

ATMOSPHERIC ENVIRONMENT

www.elsevier.com/locate/atmosenv

Airborne analysis of the Los Angeles aerosol

D.R. Collins[a], H.H. Jonsson[b], H. Liao[a], R.C. Flagan[a], J.H. Seinfeld[a,*], K.J. Noone[c], S.V. Hering[d]

[a]*Department of Chemical Engineering, California Institute of Technology, Mail code 210-41, 1200 E. Calfornia Blvd., Pasadena, CA 91125, USA*

[b]*Naval Postgraduate School, Monterey, CA, USA*

[c]*Stockholm University, Sweden*

[d]*Aerosol Dynamics, Inc., Berkeley CA, USA*

Received 17 December 1999; received in revised form 22 March 2000; accepted 30 March 2000

Abstract

As part of the Southern California ozone study (SCOS), a research aircraft was employed during August and September of 1997 to characterize the physical and chemical properties of the aerosol present over the Los Angeles Basin. Aerosol size distributions measured using a differential mobility analyzer and two optical particle counters were combined with filter-based composition measurements to derive a physicochemical description of the aerosol sampled. The accuracy of this description was evaluated through comparison of derived and directly measured aerosol properties including mass, absorption coefficient, hemispherical backscattering coefficient, and total scattering coefficient at two different relative humidities. The sampled aerosol exhibited a complex vertical structure possessing multiple elevated aerosol layers. The most pronounced of these layers were observed to form by injection of aerosol above the ground-level mixed layer along the southern edge of the San Gabriel Mountains, which form the northern boundary of much of the Los Angeles Basin. Over multiple inland areas, additional layers were observed at about 2500 m above sea level (asl), while off the coast of Santa Monica, thin but concentrated layers were detected about 500 m asl. In addition to the sharp vertical gradients in aerosol concentration observed, horizontal gradients at multiple locations were found to be sufficient to result in more than 50% variability within a 5×5 km computational grid cell commonly used in atmospheric models. Vertically resolved aerosol measurements made over one location during several flights, as well as over several locations during a morning and afternoon flight on the same day, were used to investigate the temporally and spatially resolved impact the aerosol had on gas-phase photolysis rates. These calculations predict that for a 10° zenith angle the sampled aerosol enhanced photolysis rates by up to about 5%, although a slight decrease was often observed near ground level.

Keywords: Aerosol sampling; Aircraft sampling; Southern California; Photolysis rates

1. Introduction

Southern California has long struggled to comply with state and federal air quality standards. Faced with a steadily increasing population and tightening ozone and particulate matter standards, further emissions reductions will be necessary. Extensive atmospheric modeling efforts have provided a means for linking specific emission control scenarios with probable air quality outcomes (see, for example, Meng et al., 1997). However, the complex terrain and meteorology associated with Southern California, coupled with inherent uncertainties in model input fields, complicates these efforts. Aircraft-based measurements (Blumenthal et al., 1978; Wakimoto and McElroy, 1986) have demonstrated that vertical transport in the Los Angeles area is not consistent with the simple representation of a mixed layer trapped below a temperature inversion. Recently, three-dimensional

* Corresponding author. Fax: +1-626-568-8743.
E-mail address: seinfeld@its.caltech.edu (J.H. Seinfeld).

1352-2310/00/$ - see front matter
PII: S1352-2310(00)00225-9

meteorological models have provided further insight into mechanisms responsible for formation of distinct pollution layers that exist above the Los Angeles Basin for extended periods of time (Lu and Turco, 1994, 1995). Successful prediction of ground-level concentrations can only be accomplished if the behavior and nature of material aloft are adequately described. In addition to the poorly characterized variation of species concentrations with altitude, strong horizontal gradients pose a unique problem for models; observed variations within a computational grid cell (typically, 5×5 km) call into question the assumption that concentrations are uniform inside a grid volume. Use of a single measurement within a grid cell to represent the entire cell can lead to uncertainties as high as 25–45%, depending on the species of interest (McNair et al., 1996).

During the summer and fall of 1987, the Southern California Air Quality Study (SCAQS) was undertaken to provide a sufficiently detailed data set to test the capabilities of available meteorological and air quality models. Data from SCAQS, particularly a small number of multi-day episodes, have served as the foundation for most of the modeling work in the years since (Pandis et al., 1992, 1993; Harley et al., 1993; Jacobson, 1997; Lurmann et al., 1997; Lu et al., 1997; Meng et al., 1998). Ten years after SCAQS, during the summer and fall of 1997, the Southern California Ozone Study (SCOS) was conducted in order to supplement the data set acquired during SCAQS by employing a network of emissions, meteorological, and air quality measurements. The stated goals of SCOS were:

1. Update and improve the existing aerometric and emission databases and model applications for representing urban-scale ozone episodes in Southern California.
2. Quantify the contributions of ozone generated from emissions in one Southern California air basin to federal and state ozone standard exceedances in neighboring air basins.
3. Apply modeling and data analysis methods to design regional ozone attainment strategies.

To satisfy goal 2, the study covered an extensive region that was roughly bounded by the Channel Islands to the west, the San Joaquin Valley to the north, and the California state border to the east and south. In all, the study encompassed approximately 53,000 square miles, although a large fraction of the measurements were made within the Los Angeles Basin. SCOS was conducted between mid-June and mid-October when the highest pollutant concentrations are usually observed in the region. However, during this campaign unusually high sea-surface temperatures caused by a significant El Niño event resulted in deeper marine layers and enhanced mixing relative to typical conditions in Southern California. Hence, air pollutant concentrations tended to be somewhat lower during this study than is common for the region.

As its name implies, the Southern California Ozone Study was conducted primarily to improve our understanding of ozone and its gas-phase precursors. A smaller, but still extensive, component of the study focused on understanding the formation and evolution of the atmospheric aerosol. The expanded monitoring network in place for the ozone study facilitated interpretation of aerosol measurements. As part of the aerosol component of SCOS, a research aircraft was utilized during August and September of 1997 to provide a three-dimensional characterization of the Los Angeles aerosol. This paper presents a description of the measurements obtained by that aircraft during the study period, and an analysis of the impact the aerosol column may have on key gas-phase photolysis rates involved in ozone production.

2. Instrumentation and analysis

Between 27 August and 12 September 1997 the Center for Interdisciplinary Remotely-Piloted Aircraft Studies (CIRPAS) *Pelican* aircraft flew 12 missions over the Los Angeles Basin. The *Pelican* is a Cessna Skymaster that has been modified by replacing the front engine with an extended nose cowling that serves as the primary instrumentation bay. The resulting pusher configuration is ideal for aerosol measurements because it minimizes the disturbance of the atmosphere prior to sampling. Optical particle counters were mounted on each of the wings, while the remaining instruments were located inside the aircraft. These latter instruments sampled from two parallel inlets, each of which included a cyclone with a nominal cut size of 2.5 μm. Since the cyclones were positioned immediately downstream of the inlet opening, little drying of the particles was likely prior to removal of the coarse mode. Table 1 contains a complete list of instruments on board the *Pelican* during SCOS.

2.1. Filter samples

The chemical composition of the aerosol was probed using a filter system employing three parallel sampling trains, each having a flow rate of $24\,\mathrm{l\,min^{-1}}$. Separate trains were used for analysis of trace metals, elemental and organic carbon, and inorganic ions. Each sampling train consisted of three identical filter cassettes, allowing sequential exposure of multiple filters through the use of cockpit-activated solenoid valves that were in-line with each of the filter cassettes. During SCOS, three sets of filter samples were taken during each of the first six flights, with two sets taken on the seventh flight. Filters were unloaded immediately following each flight and remained refrigerated during storage and transport until

Table 1
Measurements made on board the *Pelican*

Property measured	Size range	Instrument	Time
Aerosol measurements			
Inorganic ions, trace metals, EC/OC, gravimetric mass	< 2.5 μm	Filter samplers	~ 1 h
Particle size	0.01–0.5 μm	TSI 3071 DMA and TSI 3010 CPC	1 min
Particle size	0.15–3.0 μm	PMS PCASP	1 s
Particle size	0.5–20 μm	PMS FSSP	1 s
3-color light scattering coefficient (total and hemispherical backscattering)	< 2.5 μm	TSI 3563 nephelometer	1 s
Light scattering/RH relationship	< 2.5 μm	UW Humidigraph (Radiance Research nephelometers)	6 s
Radiation measurements			
Total solar		Eppley pyranometer	1 s
UV		Eppley radiometer	1 s
Meteorological measurements			
Pressure (static and dynamic), temperature, and dew point		Various	1 s

analysis. Several filter blanks were taken from each sampling train and were used to correct for the samples analyzed.

The first sampling train used a Teflon filter to collect samples for trace metal analysis. Inductively coupled plasma mass spectrometry (ICP-MS) was used to quantify Na^+, Al^{3+}, K^+, Ni^{2+}, Zn^{2+}, Mg^{2+}, Si^{4+}, Fe^{3+}, and Cu^{2+} for each of the filters. With the exception of Na^+ and Mg^{2+} that were assumed to be associated with sea-salt particles, each of the metals was assumed to be present as oxides (Al_2O_3, SiO_2, K_2O, Fe_2O_3, NiO, CuO, and ZnO) for determination of aerosol mass. Uncertainty in total aerosol mass introduced as a result of this assumption is relatively low since the elements analyzed typically constituted only a small fraction of the aerosol.

Elemental and organic carbon collected on quartz filters in the second sampling train was analyzed through thermal optical reflectance (Chow et al., 1993) by researchers at the Desert Research Institute (DRI). To account for the positive artifact resulting from organic vapor adsorption on the filter, a quartz back-up filter was used, with the corrected organic aerosol mass assumed to be the difference between that measured on the front and back filters. Since oxygen and hydrogen are not detected in this type of analysis, organic carbon loadings were multiplied by 1.4 to estimate total organic aerosol mass (White, 1990).

The final sampling train employed an MgO denuder to remove nitric acid in order to minimize the positive artifact that it might otherwise cause. Downstream of the denuder, a Teflon filter was used to collect aerosol for inorganic ion analysis. Researchers with DRI used ion chromatography to analyze SO_4^{2-} and NO_3^-, and colorimetry to quantify NH_4^+. The NO_3^- mass measured on the nylon back-up filter was assumed to be volatilized ammonium nitrate, and was, therefore, used to correct the NH_4^+ and NO_3^- mass measured on the Teflon filter.

To assess the degree to which the aerosol mass was accounted for through the speciation analyses, the Teflon filters collected were analyzed by gravimetry. These analyses were conducted by researchers at DRI under controlled conditions in which the relative humidity was maintained at between 45 and 55%. The correction applied to the NH_4^+ and NO_3^- concentrations to account for ammonium nitrate volatilization was also applied to the gravimetric mass.

Detection limits for each aerosol species analyzed are listed in Table 2. Aerosol mass for each of the 20 sets of filters analyzed is shown in Fig. 1. With the exception of the flights of 4 and 5 September, filter samples represent the integration of the aerosol present over a relatively wide area and over about 2 km variation in altitude.

Table 2
Detection limits for species analyzed

Species	Analytical limit (μg filter^{-1})	Ambient concentration (μg m^{-3})
SO_4^{2-}, NO_3^-, NH_4^+	0.8	0.4
OC	2	1
EC	0.5	0.3
Fe, Si, K	0.1	0.05
Na	0.01	0.005
Mg, Ni, Cu, Zn, Al	0.001	0.0005
Mass	10	5

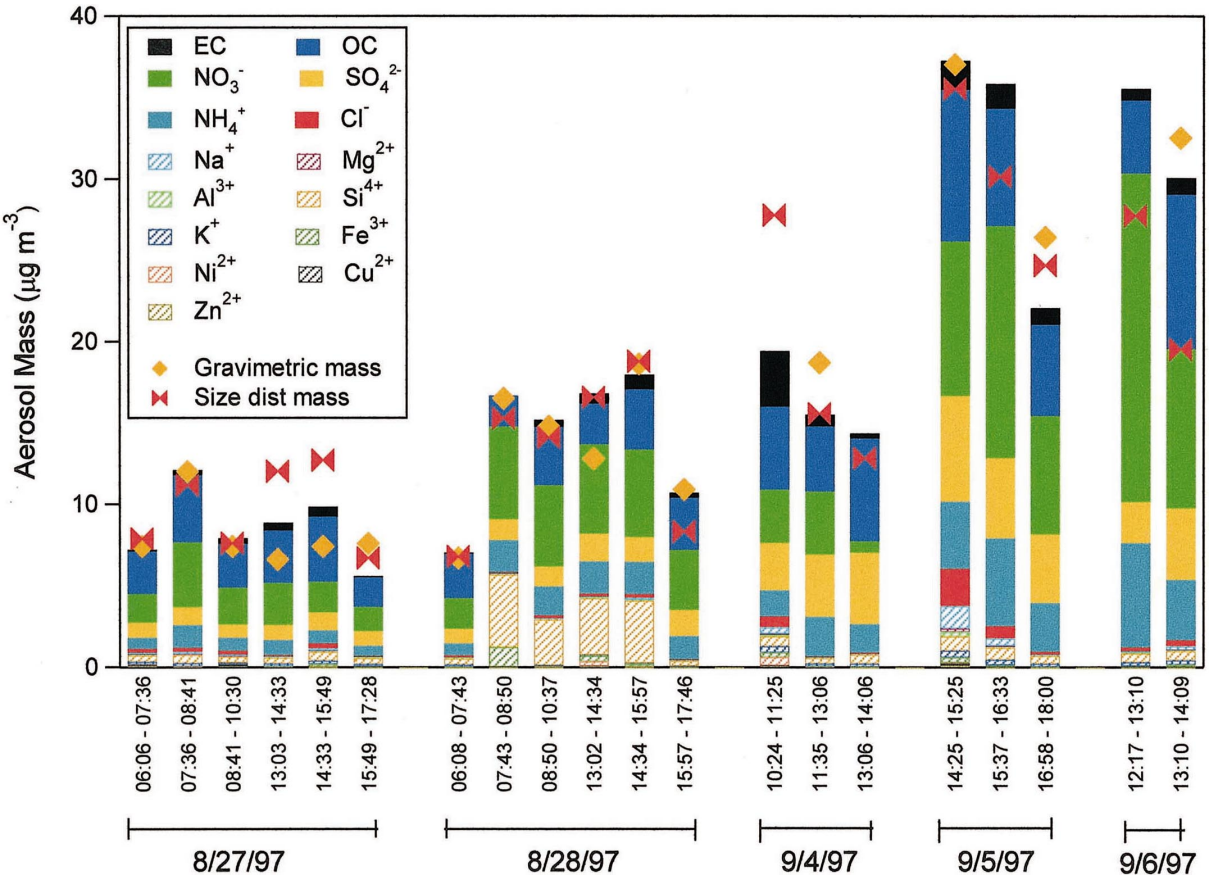

Fig. 1. Fine ($D_p < 2.5$ μm) aerosol chemical composition during the seven flights for which samples were collected. Also shown is aerosol mass determined gravimetrically, and through integration of the size distributions.

These spatially unresolved filter measurements were used to gain a general understanding of the chemical nature of the aerosol and to aid in the analysis of time-resolved size distributions, but were not used to directly assess variations in composition within the study area.

2.2. Optical measurements

Three integrating nephelometers and an absorption photometer provided details of the optical and hygroscopic properties of the aerosol sampled during SCOS. The University of Washington Passive Humidigraph, which consists of two Radiance Research nephelometers operated in parallel at different relative humidities (RH), was used to investigate the relationship between humidity and aerosol light scattering. In general, humidities within the dry and wet nephelometers bracketed the ambient RH. A TSI 3563 nephelometer that measures total scattering and hemispherical backscattering at blue (450 nm), green (550 nm), and red (700 nm) wavelengths was operated at a humidity slightly below that of the drier of the two Radiance Research nephelometers. Each of the nephelometers was calibrated prior to, or during, the study using gases with known scattering properties.

A Radiance Research particle soot absorption photometer (PSAP) was used to make time-resolved measurements of the absorption properties of the dry aerosol. The PSAP continuously records transmittance of light (567 nm) through two regions on a filter, one of which has an aerosol-laden flow passing through it, while the other is used as a reference. The aerosol absorption coefficient, σ_{ap}, is determined from the rate of change of the transmittance ratio between the two regions. PSAP calibration results described by Bond et al. (1999) were used to analyze the data obtained. It has been observed that variations in transmittance ratio unrelated to increased particle loading occur as a result of pressure variations within the instrument. Only during constant altitude legs when the observed change in transmittance due to particle loading dominated over that caused by pressure variations were data analyzed.

2.3. Size distribution measurements

By integrating measurements from a differential mobility analyzer (DMA) and two optical particle counters (OPCs), aerosol size distributions spanning the range from 10 nm to $> 20\,\mu m$ in diameter were determined with 1 min time resolution. A TSI 3071 cylindrical DMA was operated with a TSI 3010 condensation particle counter to size particles with diameters between approximately 10 and 500 nm. Each of the DMA flow rates was actively controlled to minimize fluctuations induced by pressure changes within the instrument. The voltage applied to the DMA was scanned over 45 s, and was automatically adjusted to maximize particle size range, while remaining below the pressure- and temperature-dependent threshold for electrostatic breakdown. A wing-mounted Particle Measuring Systems (PMS) passive cavity aerosol spectrometer probe (PCASP-100×) sized particles ranging from approximately 140 nm to over 3 μm. The PCASP was calibrated prior to SCOS with polystyrene latex (PSL) particles. Mie Theory calculations that accounted for the angular configuration of the light receptor in the PCASP were used to adjust this PSL calibration to that expected for particles of any specified complex index of refraction. Mounted on the wing opposite to the PCASP was a PMS forward scattering spectrometer probe (FSSP-100). By utilizing an external laser/detector, the FSSP causes only minimal disturbance to large particles and cloud droplets. The 1 Hz measurements of both the PCASP and FSSP were averaged over the ~ 1 min measurement time of the DMA.

The PCASP and DMA systems both change the relative humidity of the aerosol during the act of sampling, while the FSSP has little effect on this important parameter. To combine these measurements into a coherent description of the sampled aerosol, the ambient particle size distribution must be estimated from the perturbed data. An accurate description of the effect of humidity on particle size requires knowledge of, or assumptions about, the aerosol composition, mixing state, and deliquescence state. Filter samples taken during the majority of the *Pelican* flights were used to estimate the composition of the sampled aerosol during the respective filter integration interval. For those flights during which no filter samples were taken, the average composition analyzed during the flights with filter measurements was used. Since filter samples were not size-resolved, it was assumed that size-dependent composition and mixing relationships were similar to those described by Zhang et al. (1993) in their analysis of data taken during SCAQS. External mixtures of salt particles were assumed so that available single-salt solution thermodynamics data (Tang and Munkelwitz, 1994; Tang, 1996; Tang et al., 1997) could be used for particle growth/evaporation calculations. Tang (1996) showed that only minor differences exist in overall optical properties of internal and external mixtures of common nitrates and sulfates. Moreover, the similar densities of common nitrates and sulfates limit the uncertainty in the calculated aerosol mass that might be caused by this assumption. Hygroscopic growth was considered only for the salt species, and not for carbon or dust. The assumption that carbonaceous aerosol is non-hygroscopic is known to be incorrect for at least some organic species found in the aerosol phase (Saxena et al., 1995). However, in their interpretation of SCAQS impactor data, Zhang et al. (1993) suggest that externally mixed carbonaceous particles were non-hygroscopic, while carbon internally mixed with salt particles was less hygroscopic than the salt itself. The relatively low humidity encountered throughout the present study, and generally characteristic of the region, further limits uncertainties caused by this assumption.

The ambient relative humidity measured during SCOS often lay between the crystallization and deliquescence points of the salt species known to be present in the aerosol. Whether the aerosol would be wet or dry under these circumstances depends on the RH history it experienced. Humidity data taken during the flights, coupled with continuous ground-based measurements at five locations in the Los Angeles area, were used to estimate the maximum humidity encountered by the aerosol that was sampled during a given flight. As an estimate of the uncertainty that this assumption might introduce, it was determined that, averaged over all of the flights, PM2.5 (dry aerosol mass $\leqslant 2.5\,\mu m$ aerodynamic diameter) calculated using the assumption that the maximum humidity encountered was the ambient humidity at that time is only 5.1% greater than that calculated assuming all salts had previously deliquesced. After adjusting for relative humidity differences, excellent agreement in measured concentration was observed in the overlapping size range of the PCASP and FSSP. In general, the size distribution recovered from the DMA had a similar shape to that measured by the PCASP, but was shifted by about 10% to larger size. The cause of the discrepancy is not known, but it generally had little impact on derived aerosol mass and optical properties. Lacking definitive evidence of the relative accuracy of the different measurements, individual distributions were simply averaged in overlapping size ranges.

2.4. Optical and mass closure

Although composition and optical measurements afford valuable information about the properties of the sampled aerosol, only an accurate physicochemical description can provide a full range of spatially and temporally resolved aerosol characteristics. In order to test the validity of the size distribution-based physicochemical description of the aerosol, a number of closure comparisons were performed with the optical and composition measurements. The utility of such comparisons

is that they provide confidence in the over-determined set of measurements when closure is achieved, and indicate potential sources of error when it is not.

To estimate aerosol mass collected on the filters during sampling intervals, aerosol size distributions were first adjusted to the relative humidity within the cyclone, which was slightly warmer and drier than outside. The density of each aerosol type considered was then calculated and used to determine the appropriate cyclone penetration efficiency s-curve. For hygroscopic particles, density was calculated as a function of relative humidity, whereas constant densities of 2.6 g cm^{-3} for dust (Tegen and Fung, 1994), and 2.0 and 1.4 g cm^{-3} for elemental and organic carbon, respectively (Larson et al., 1988), were used. The aerosol mass of those particles that passed through the cyclone was then calculated through integration of the size distribution. Aerosol mass derived in this way is included in Fig. 1. Although there are some differences between the three measures (species sum, gravimetric, and size distribution integration) of aerosol mass during a given filter interval, there are no pronounced systematic discrepancies.

As with aerosol mass calculations, modification of the aerosol size distribution to account for removal in the cyclone is necessary for comparison with the various optical instruments on board. The remaining particles are then adjusted to the relative humidity within each instrument. For those cases in which the relative humidity of the sample flow is reduced below the crystallization point of a given salt, only if the RH in the humidified nephelometer is above the deliquescence point of the salt is it assumed to be hydrated. For analysis of scattering and absorption coefficients, constant refractive indices of 1.95–0.66i for elemental carbon (Bergstrom, 1972) and 1.55–0.0i for organic carbon (Larson et al., 1988) were assumed. The wavelength-dependent complex index of refraction of Saharan dust particles described by Patterson et al. (1977) was assumed to be representative of dust present in Los Angeles. Optical properties of dust vary with location and even time, but few representative data are available. Fortunately, the contribution of dust to scattering and absorption was generally small, minimizing the uncertainty in derived optical properties resulting from this assumption. Refractive index of aqueous aerosols was determined by the partial molal refraction approach of Moelwyn-Hughes (1961). For internal mixtures of salt and carbon, the volume-weighted average of the refractive indices of the components was used. Fuller et al. (1999) found that volume-weighted calculations tend to overestimate absorption of a mixed salt/elemental carbon particle relative to more physically realistic scenarios such as a salt shell that contains an elemental carbon inclusion. However, because of uncertainty in the mixing state and size distribution of carbon in the aerosol, the magnitude of the error remains unknown.

Mie Theory was used to predict the response of the optical instruments to the sampled aerosol with specified size-resolved concentration and refractive index. For comparison with the nephelometers, the angular sensitivity of the TSI 3563 (Anderson et al., 1996) was incorporated into the Mie Theory calculations. Fig. 2 shows closure comparisons with the total scattering coefficient measured by each of the Radiance Research nephelometers, the 550 nm hemispherical backscattering coefficient measured by the TSI nephelometer, and the absorption coefficient measured by the PSAP. Data from each of the seven flights during which filter samples were taken are included in the comparisons with the three nephelometers, while data from only those flights that included extended constant altitude legs were included in the PSAP comparison to minimize biases caused by pressure variations. Although each comparison is characterized by some discrepancy, that with the PSAP is clearly the most significant. Potential causes of this disagreement include errors in the analysis of carbon or in the distinction between organic and elemental carbon, errors in assumed mixing state and sphericity of the particles, and errors in the absorption measurement itself, potentially due to the broadside enhancement effect described by Fuller et al. (1999). It is unlikely that this discrepancy results from use of volume-weighted refractive indices in the size distribution-based calculations, since this would tend to increase the derived absorption coefficient, thereby improving agreement.

3. Three-dimensional aerosol structure

A variety of flight patterns were utilized during SCOS in order to explore the three-dimensional distribution of the aerosol in the Los Angeles Basin. The pattern used during the first four missions of SCOS consisted of a sequence of ascending and descending spirals. Both spatial and temporal variations in the aerosol were explored by conducting one of these 4-h missions in the morning and another in the afternoon on both 27 and 28 August. Meteorological measurements showed the temperature inversion on 27 August had a height of approximately 350 m until breaking up in the early afternoon. A weak offshore flow was observed during the evening, followed by onshore flow and an inversion having a height of approximately 500 m the following day. Peak 1-h ozone concentrations observed in the Southern California Air Basin were 116 and 132 ppb on 27 and 28 August, respectively.

To present the three-dimensional structure of the aerosol during this period, data from spirals along two cross sections have been considered. An east–west cross section was chosen that includes spirals over Santa Monica, El Monte, Azusa, Pomona, and Rialto, while a north–south cross section includes spirals over Altadena, El Monte,

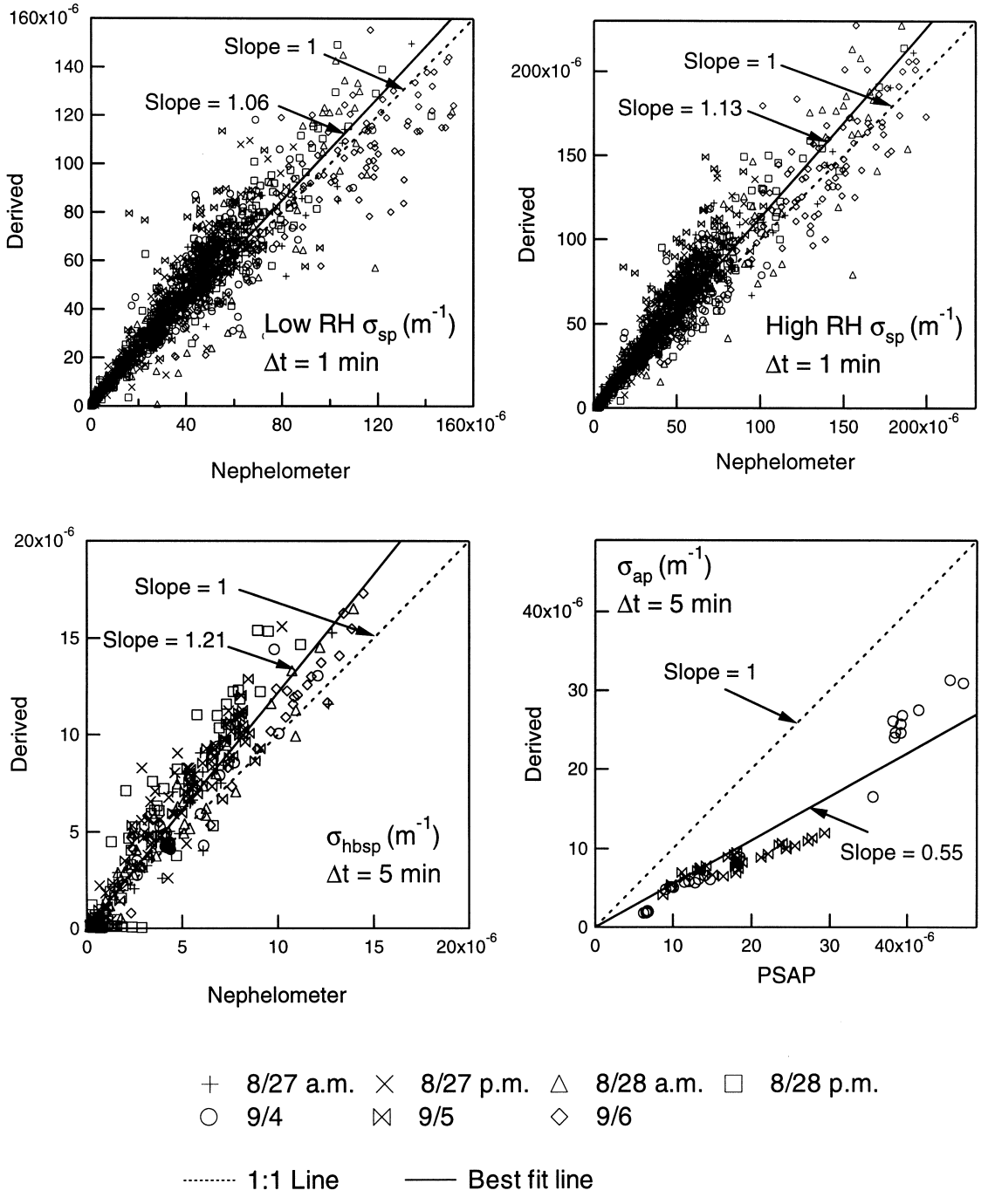

Fig. 2. Closure comparisons between derived and directly measured optical properties. Data presented are from those flights during which filter samples were collected. Comparisons shown include total scattering coefficients measured by the Radiance Research nephelometers at varying relative humidity, hemispherical backscattering at 550 nm measured by the TSI nephelometer, and absorption measured by the PSAP.

Fullerton, and Seal Beach. It is not possible to completely deconvolute the spatial variations between spiral locations from variations that result from evolution or advection of the aerosol during the course of a flight. Nor is it possible to predict with confidence the aerosol properties at a point along one of the cross sections through simple interpolation of measurements made. Nevertheless, Figs. 3 and 4 present data along these cross sections

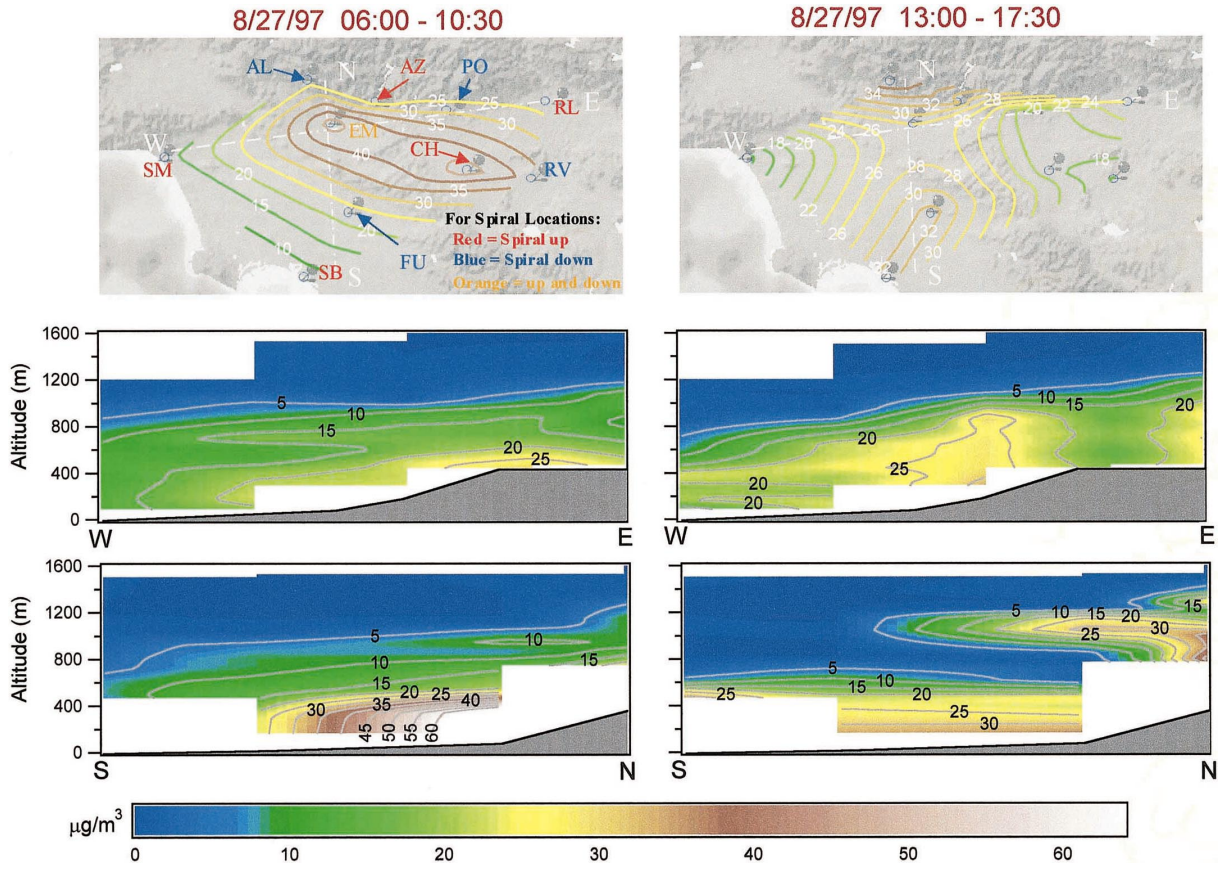

Fig. 3. Distribution of PM2.5 throughout the Los Angeles basin as sampled during morning and afternoon flights on 27 August. The top plots show contours of near-ground-level aerosol mass as well as the east–west (E–W) and north–south (N–S) cross sections used in the image plots shown below. As indicated in the 27 August contour plot, spiral locations are Altadena (AL), Azusa (AZ), Chino (CH), El Monte (EM), Fullerton (FU), Pomona (PO), Rialto (RL), Riverside (RV), Santa Monica (SM), and Seal Beach (SB). Represented in the image plots is PM2.5 interpolated from adjacent spirals. The solid gray area at the bottom of each of the image plots represents the approximate ground level.

as if they were snapshots in time exhibiting smooth variations between locations. PM2.5 has been considered here because of its regulatory relevance. Shown at the top of these figures are contour plots of aerosol mass derived from measurements made at the lowest point of each spiral. Also presented are the east–west (E–W) and north–south (N–S) cross sections considered. Beginning on the morning of 27 August, the aerosol was most concentrated over the inland valleys between El Monte and Chino, where PM2.5 exceeded 40 $\mu g\,m^{-3}$. Strong gradients in PM2.5 are apparent along both cross sections between the coast and inland areas. Only a weak aerosol layer at approximately 1000 m above sea level (asl) is visible above the ground-level polluted layer. Along the east–west cross section, little change is observed in near-ground-level aerosol mass from morning to afternoon, although the columnar aerosol burden over the inland areas increased, and a weak, but distinct, layer at $\sim$400 m asl developed that stretched to Santa Monica. At approximately 1200 m asl along the north–south cross section, a much more intense aerosol layer is observed, in which PM2.5 exceeds 30 $\mu g\,m^{-3}$. These data suggest that aerosol was injected above the mixed layer at the southern edge of the San Gabriel Mountains and was then transported away from the mountains with the sea breeze return flow. Aircraft-based measurements have previously identified such elevated pollution layers both over Southern California (Blumenthal et al., 1978; Wakimoto and McElroy, 1986; Li et al., 1997) and over similar coastal regions (Wakamatsu et al., 1983; Lalas et al., 1983; Hoff et al., 1997). A second, less pronounced, layer is present approximately 200 m above the first. The two layers present along the east–west cross section the following morning are likely remnants of this

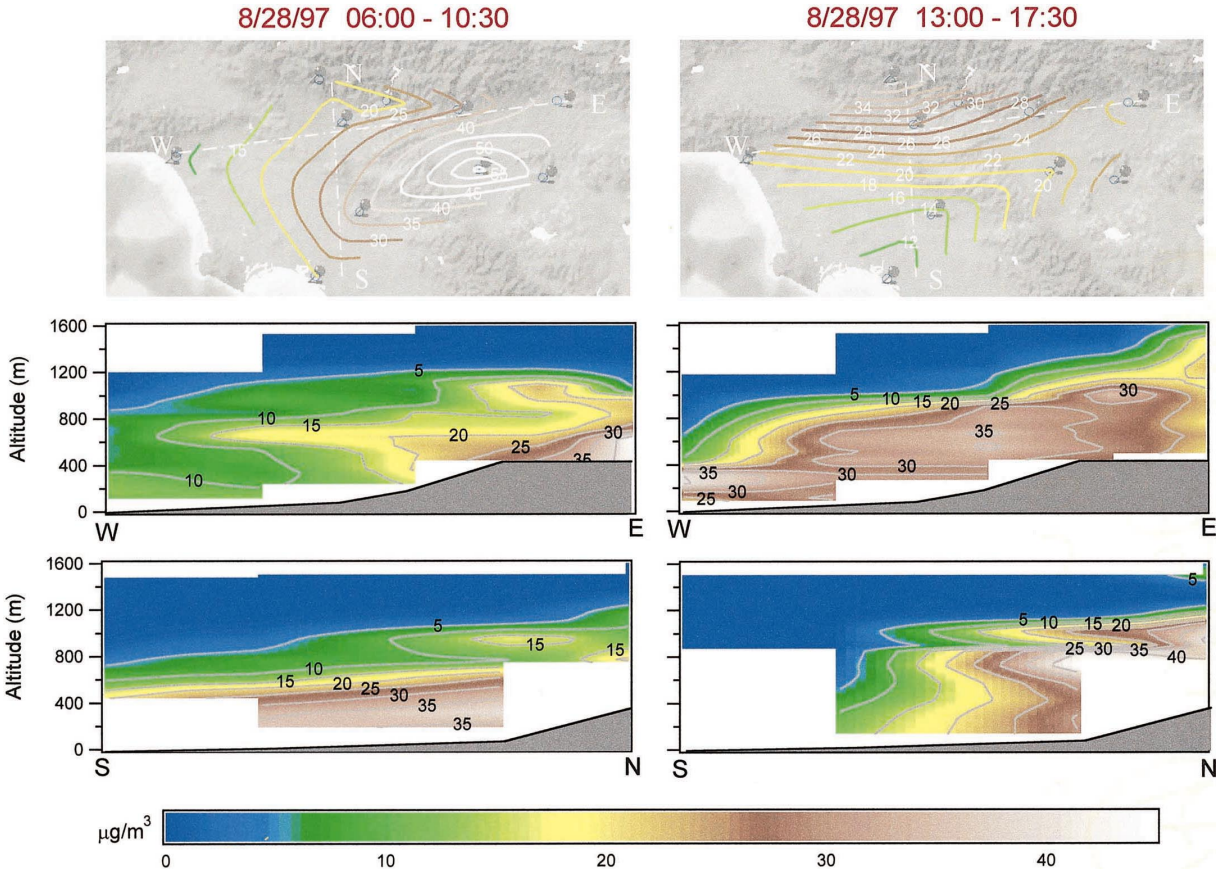

Fig. 4. The same format as in Fig. 3 for the aerosol sampled during morning and afternoon flights on 28 August.

(these) layer(s). As the ground-level mixed layer deepens in the afternoon of 28 August, the morning layers cease to be distinct, suggesting that they mixed with the underlying layer. Along the north–south cross section, an elevated layer formed on 28 August in much the same way as was observed the previous day.

The climb and descent rates used during this study were typically 150 m min^{-1}, leading to a vertical resolution of $\sim$ 150 m in the size distribution measurements. Aliasing due to this limited vertical resolution became excessive during several spirals, in which case the faster nephelometer measurements were examined. Fig. 5 shows aerosol scattering coefficients recorded with the non-humidified Radiance Research nephelometer during each of the spirals flown off the coast of Santa Monica on the first four flights. The morning spirals show relatively little vertical variation on either day. With the strengthening of the sea breeze in the afternoon, pronounced, but thin ($\sim$ 100 m), aerosol layers developed. The scattering coefficient of 0.00014 m^{-1} measured in the August 28 layer was among the highest observed at any location during the study. Like the layers over the inland areas, these coastal layers have been observed in previous studies and are attributed to vertical transport along the heated coastal ranges, followed by horizontal transport towards the coast as part of the sea breeze return flow (Lu and Turco, 1994).

During one flight on 9 September and two flights the following day three spirals over El Monte and two over Long Beach reached altitudes of over 3000 m. On both of these days upper level winds were from the south and west, and temperature inversions were present until mid-afternoon. Maximum 1-h ozone concentrations were 105 and 113 ppb on 9 and 10 September, respectively. Though the spirals were flown over a 32-h period at two dissimilar locations, each encountered an aerosol layer at approximately 2500 m having a peak PM2.5 mass of about 2 μg m^{-3}, as shown in Fig. 6a. The early morning spiral flown over El Monte on 9 September indicates that a more concentrated layer may have been present above 3000 m, although no similar layers were observed during 3400 m spirals on the morning of 10 September. The

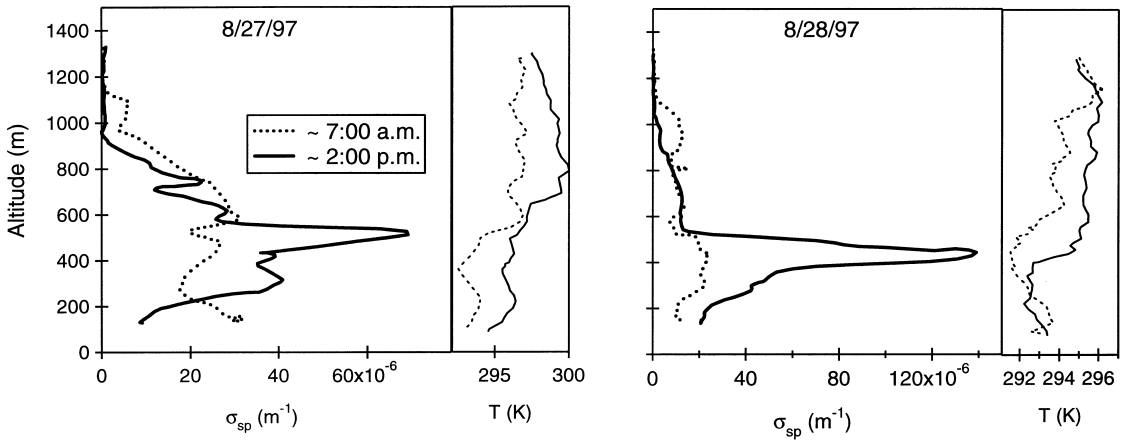

Fig. 5. Vertical profiles of ambient temperature and aerosol scattering coefficient measured during spirals flown off the coast of Santa Monica on four missions conducted on 27 and 28 August.

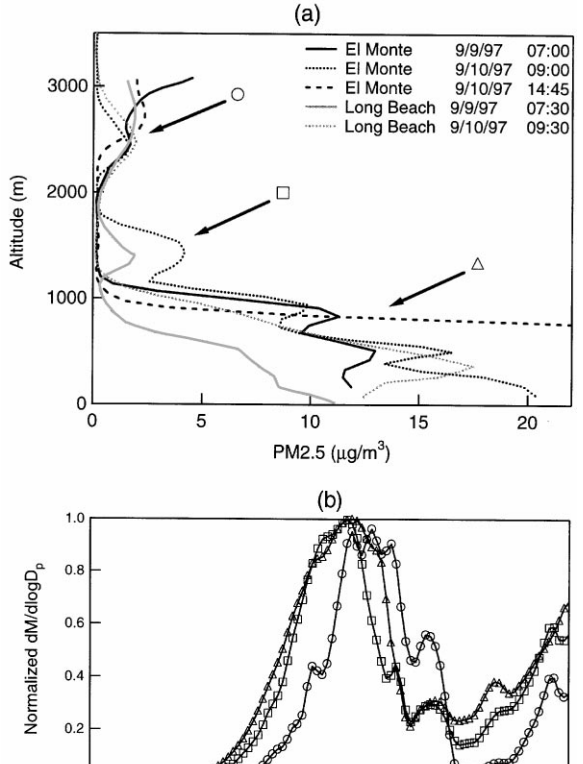

Fig. 6. (a) Vertical profiles of PM2.5 measured during 3000 + m spirals flown over El Monte and Long Beach, and (b) normalized mass size distributions averaged over each of the layers indicated by arrows in (a).

averaged mass distributions for the layers indicated by arrows in Fig. 6a are presented in Fig. 6b. There is a clear shift in the aerosol mass distribution within the 2500 m layer relative to the aerosol within either the ground level or 1500 m layers. This observation is consistent with an aerosol that has aged through condensation and coagulation.

Seven different flight patterns were employed for the 12 missions flown during SCOS, making analysis of day-to-day variations difficult. However, the majority of flight patterns included spirals over El Monte, Riverside, and Fullerton. These repeated spirals provide the data necessary for a statistical analysis of the aerosol over these locations. Day-to-day variations in the aerosol concentration and properties obscured any diurnal trends that might otherwise have been apparent. Therefore, in combining data from each set of spirals, no distinction was made between samples taken at different times. Fig. 7 presents the mean and standard deviation of several intensive and extensive aerosol properties as a function of altitude for 10 spirals flown over both El Monte and Riverside, and 9 flown over Fullerton. The data have been smoothed to more clearly show vertical trends. As indicated in these plots, the aerosol variability at each location exceeds the mean variability between locations. Consistent with expectations, aerosol mass decreases with increasing altitude and with proximity to the coast. Aerosol number concentration was about 50% higher in El Monte than in Riverside, while aerosol mass was higher in Riverside, indicating that much of this increased mass results from growth of existing particles. Steadily improving air quality in Los Angeles, coupled with atypical meteorology associated with a strong El Niño event, led to significantly lower aerosol loadings

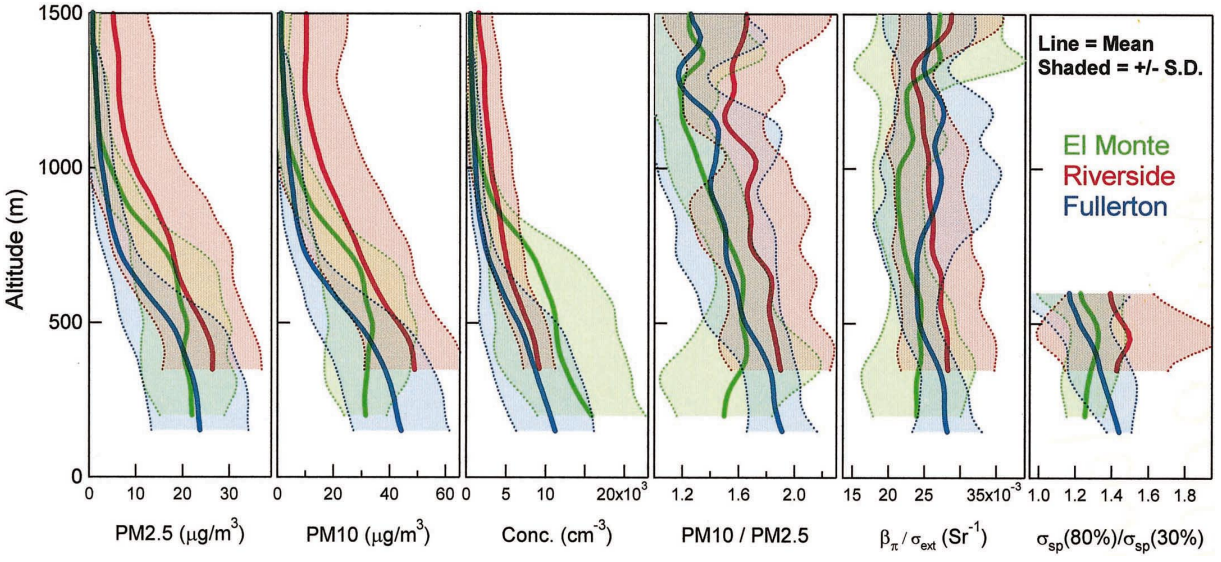

Fig. 7. Vertical profiles representing the mean and standard deviation of a number of extensive and intensive aerosol properties. Data taken during the 10 flights during which spirals were flown over El Monte and Riverside, and 9 flights with spirals flown over Fullerton were used in the analysis. For the derived ratio of scattering at 80% RH to scattering at 30% RH, only those data below the altitude at which random error began to dominate are shown.

during SCOS than during SCAQS 10 years earlier. However, the relative contributions of fine (PM2.5) and coarse (PM10–PM2.5) fractions remained much the same. Chow et al. (1994) found that, during SCAQS, PM2.5 constituted between 50 and 67% of PM10, while near-ground-level measurements made on board the *Pelican* during SCOS indicate a corresponding range of 53–69%. At each of these locations, PM2.5 constituted an increasing percentage of PM10 with increasing altitude. The ratio of aerosol scattering at 80% RH to that at 30% RH is derived using the data from Radiance Research nephelometers along with an empirical relationship between scattering intensity and RH (Kasten, 1969). Only those data below the altitude at which random error began to dominate this ratio are shown. The enhanced ratio observed for Riverside suggests that aerosol hygroscopicity is greater in the inland areas, although variations in aerosol size distribution could also account for the change.

4. Sub-grid variability

The primary goal of SCOS was the acquisition of a sufficiently detailed database to lead to effective evaluation of photochemical and aerosol modeling capabilities. Computational limitations, sparse meteorological and air quality measurements, and limited emissions inventories all serve to limit the minimum useful computational grid size of three-dimensional models. Typical grid cells are 5 km on a side with a vertical dimension that varies with height (Meng et al., 1997). McNair et al. (1996) discuss potential errors involved in assuming that point measurements of a given species represent the grid cell volume average. In their analysis of data obtained during SCAQS, they found that for the one pair of monitoring sites that were separated by less than 5 km (4.8 km), variations in peak ozone concentration of up to 50% were observed. Similar discrepancies were noted when point measurements were compared with interpolations between surrounding measurements.

Identical patterns were flown on 4 and 5 September as part of an intensive measurement period during SCOS that was designed to investigate nitrate formation along a trajectory beginning east of downtown Los Angeles in Diamond Bar, passing over the ammonia-rich area near Mira Loma, and ending near the eastern edge of the Los Angeles Basin in Riverside. Meteorological measurements describe an initial offshore flow on 4 September that gave way to onshore winds and a 120–150 m deep marine layer on 5 September. This transition was largely the result of increasing influence of tropical storm Kevin off the tip of the Baja Peninsula. Peak 1-h ozone concentrations diminished with this transition from 157 ppb on 4 September to 113 ppb on 5 September. To ensure a sufficient amount of aerosol was collected for filter analyses, the *Pelican* circled $\sim$ 300 m above each sampling site for approximately 1 h. Fig. 8 shows flight patterns for these missions. Inspection of data from these flights during some of the constant altitude circular flight

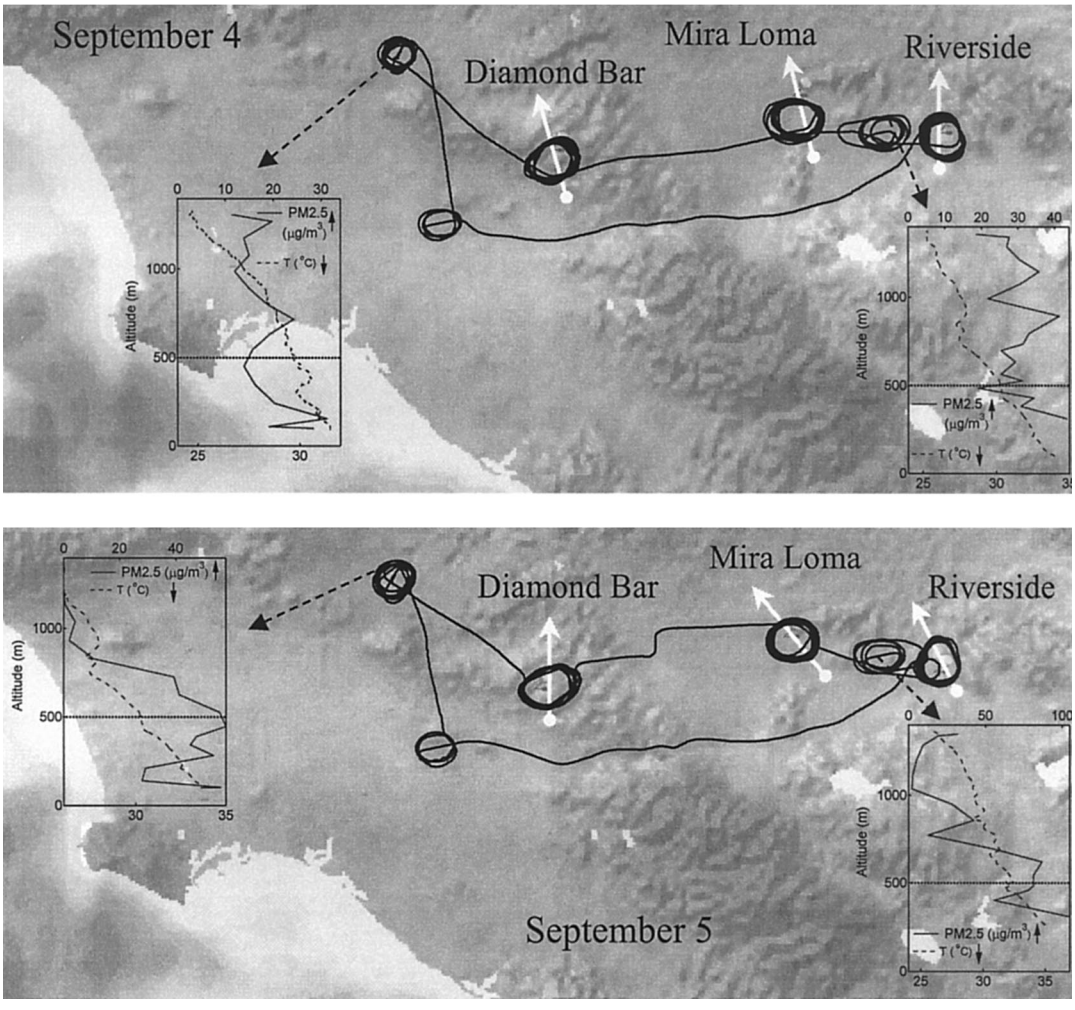

Fig. 8. Flight patterns for missions conducted on 4 and 5 September. Insets show vertical profiles of PM2.5 and temperature at spiral locations. The heavy horizontal line in each of the profiles represents the approximate altitude of the circles flown above Diamond Bar, Mira Loma, and Riverside. The solid arrows through the flight track represent the direction of maximum aerosol gradient at each of the sampling locations that was used for the analysis presented in Figs. 9 and 10.

patterns showed persistent gradients in aerosol concentration. The diameter of the circles ranged from about 5.5 to 6.5 km. This is comparable to the computational grid size of conventional three-dimensional models. Unlike simultaneous ground-based samples at multiple locations, airborne analysis of relative changes in pollutant concentrations is largely insensitive to instrumental variability. On the other hand, with aircraft sampling it is possible that variations perceived as being attributable to horizontal gradients could, in fact, result from sampling along the boundary of a vertical layer that varies in height. Because of flight pattern restrictions, spirals were not flown over any of the sampling locations, but were flown above adjacent areas. As shown in the insets in Fig. 8, vertical profiles of PM2.5 and temperature over El Monte and Riverside do not indicate the presence of sharp vertical gradients near the sampling altitude ($\sim$ 500 m), suggesting that any variations are horizontal in nature.

For each sampling location shown in Fig. 8, an arrow indicates the direction corresponding to the maximum gradient in aerosol concentration. Figs. 9 and 10 show variations along the indicated direction of maximum gradient of several normalized extensive and intensive aerosol properties, as well as size distributions. The data along the gradients were averaged to limit scatter. Some variability was apparent at each location, but that observed at Diamond Bar and Mira Loma on 4 September

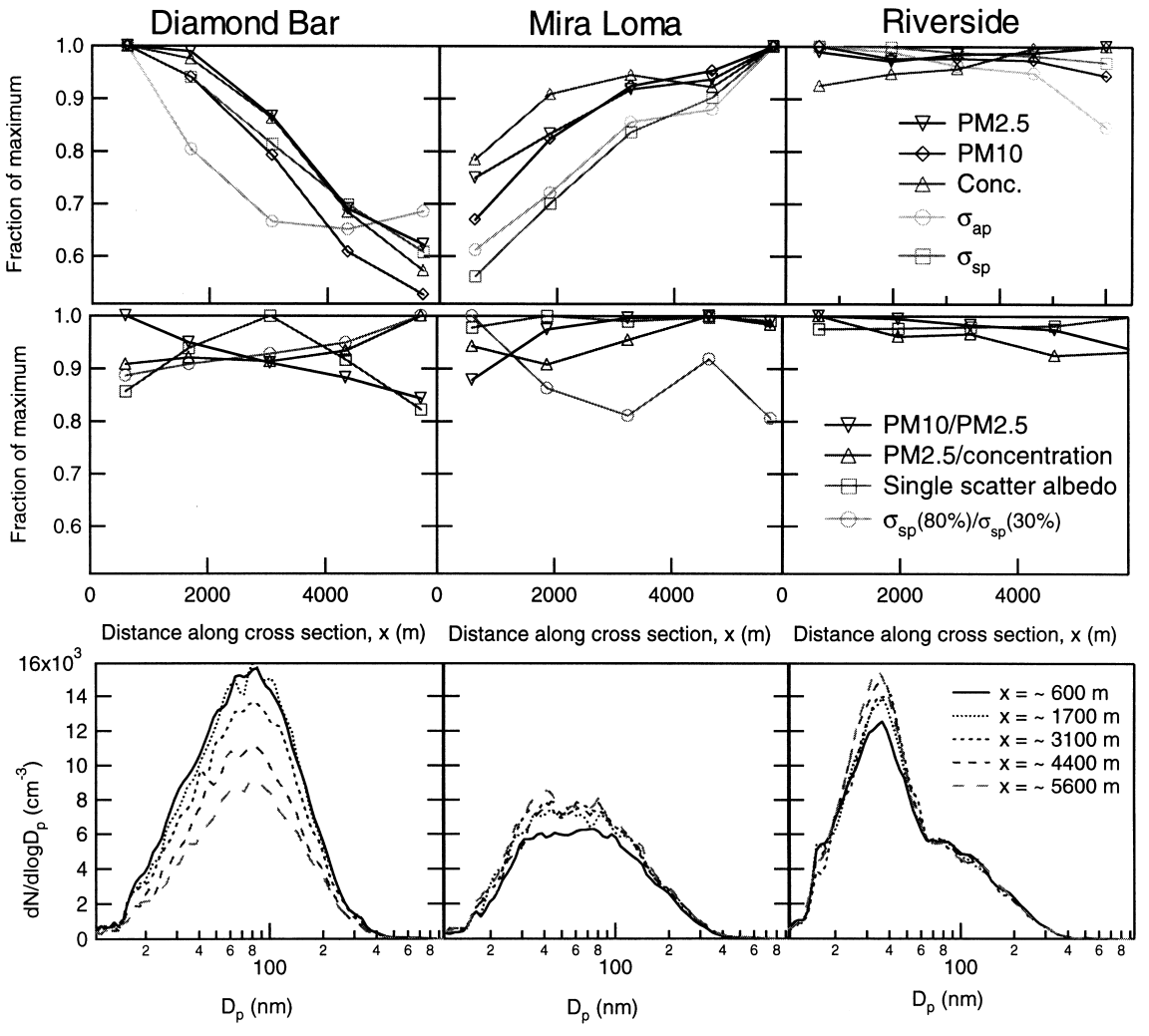

Fig. 9. Variation of extensive aerosol properties, intensive aerosol properties, and number size distributions as a function of distance along the direction of maximum gradient indicated in Fig. 8.

and Riverside on 5 September is consistent with the presence of strong gradients in aerosol concentration, resulting in $PM2.5_{max}$: $PM2.5_{min}$ ratios of 1.61, 1.33, and 1.39, respectively. The lack of variability in either the intensive properties or the shape of the size distributions suggests that the aerosol concentration varies with location, but its characteristics do not. As is true for most of the Los Angeles Basin, there are major freeways as well as other emissions sources in the vicinity of each of these locations, potentially causing the observed variability. It is also possible that the variability is a result of changes in boundary layer depth over the area of the orbit. It is interesting to note that none of the locations exhibited the same variability, or lack thereof, on both days. Additional measurements are necessary to determine whether the presence of these strong gradients follows a diurnal pattern, which might explain the differences observed over the two-day period since the 4 September mission was conducted approximately 4 h earlier than the flight conducted on 5 September.

5. Effect of the aerosol on photolysis rates

Formation of ozone and a number of other gas and aerosol phase species is driven by photochemistry (Seinfeld and Pandis, 1998). Accurate prediction of gas-phase concentrations requires a detailed understanding of the array of reactions responsible for their formation and destruction, as well as the spectrally resolved actinic flux throughout the area of interest. Direct measurement of actinic flux or key photolysis rates themselves can

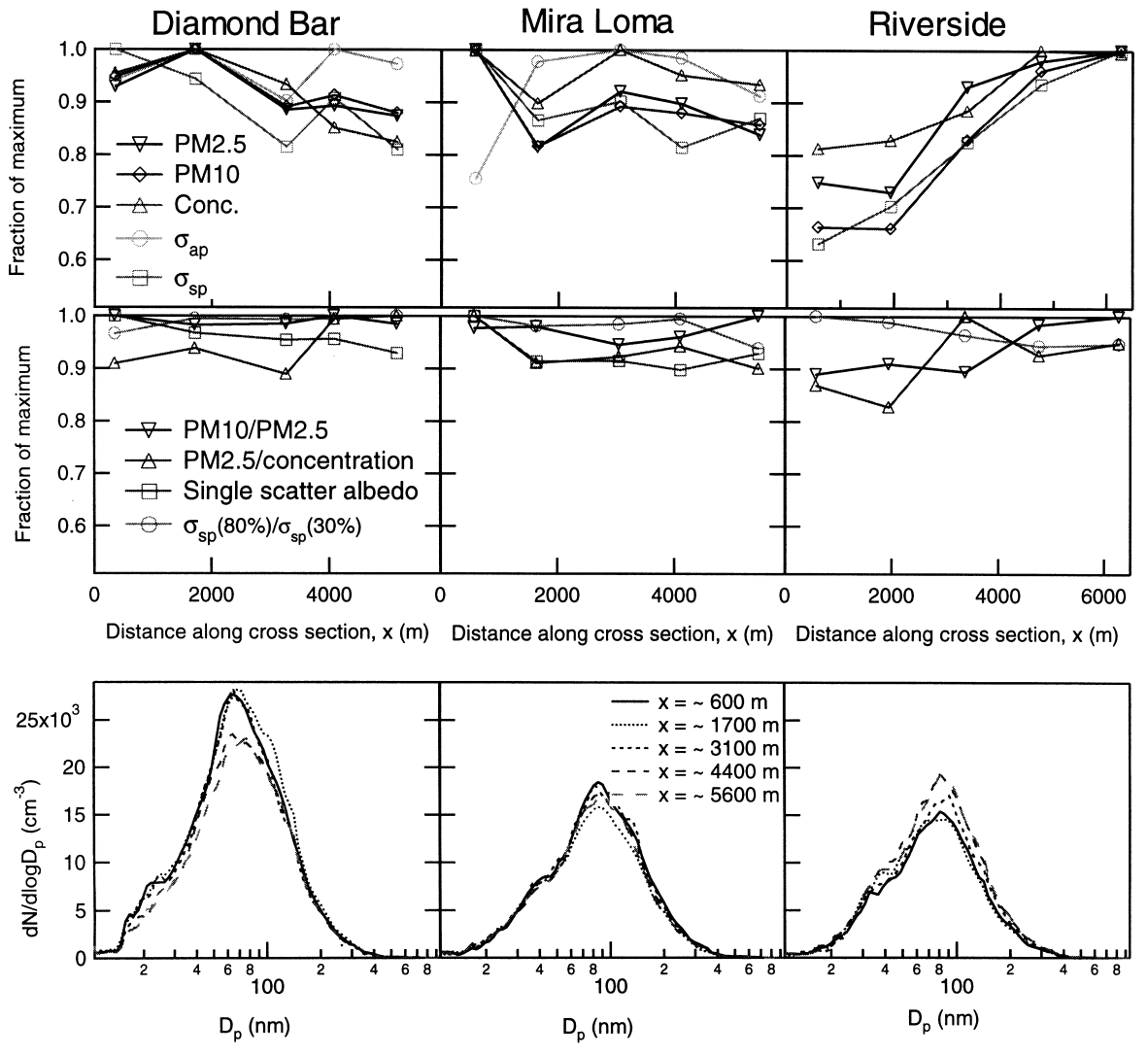

Fig. 10. The same format as in Fig. 9 for the aerosol sampled on 5 September.

provide the necessary information, although such data are typically available only at ground level. Alternatively, vertical aerosol profiles derived from airborne measurements or vertically resolved models can be used to determine the potential impact of scattering and absorption on photolysis rates. Several investigations of this type have been reported for different regions with varying cloud cover, surface albedo, and solar zenith angle (Demerjian et al., 1980; Ruggaber et al., 1994; Lantz et al., 1996; Castro et al., 1997; Dickerson et al., 1997; Jacobson, 1998; Liao et al., 1999). The extensive aerosol measurements made with the *Pelican* provide much of the data necessary for such an analysis, thereby reducing uncertainty in the role of the aerosol in atmospheric photochemistry.

The approach taken here to determine photolysis rates has been described in Liao et al. (1999), and will be described only briefly. Actinic flux was calculated using the one-dimensional discrete ordinate radiative transfer (DISTORT) model (Stamnes et al., 1988). The calculations employed 80 vertical layers from 0 to 70 km that ranged in thickness from 100 m in the lowest 3 km, to 5 km between 50 and 70 km in altitude. Aerosol concentration was assumed to be zero above the maximum measurement height. Clearly, this will result in some error in derived photolysis rates. An analysis of the impact of the layers observed at about 2500 m will be discussed below, but no consideration of even higher layers is made, although it is likely that the aerosol present above this height contributes negligibly to the

columnar aerosol burden. Actinic flux was calculated for the 290–700 nm wavelength range with spectral intervals ranging from 1 nm for wavelengths between 290 and 330 nm, to 5 nm between 600 and 700 nm. Published data for temperature-dependent ozone absorption cross section (Malicet et al., 1995; WMO, 1985), solar irradiance (Neckel and Labs, 1984; Woods et al., 1996), temperature profile (Nagatani and Rosenfield, 1993), ozone profile (McPeters, 1993), and spectrally resolved surface albedo (Demerjian et al., 1980) were utilized for these analyses. As is common in Southern California during the summer months, clouds were rare during this study and were, therefore, not considered. To clearly demonstrate the variability associated with aerosol concentration and properties, and not time of day, a constant solar zenith angle of 10° was considered.

Consistent with the approach taken to characterize physical and chemical aerosol properties, photolysis rates were computed based on data taken along a cross section during one flight, and taken at one location during several flights. Poor spectral resolution and size-dependent non-idealities prevented direct use of nephelometer and absorption photometer measurements. Instead, aerosol optical properties at each height interval were determined through Mie Theory calculations using the size distributions. As discussed above, the size distribution measurements have vertical resolution of approximately 150 m, which is slightly greater than the minimum vertical layer thickness used in DISORT, so limited interpolation was necessary. The fractional change in several key photolysis rates resulting from the aerosol sampled over El Monte during 10 flights is presented in Fig. 11. As with the statistical analysis of vertically resolved aerosol properties shown in Fig. 7, the mean and standard deviation were calculated and presented as a solid line and shaded region, respectively. Little variation is observed in the impact the aerosol is expected to have on photolysis rates of NO_2, HCHO, CH_3COCH_3, and $O_3 \rightarrow O(^1D)$, while the impact on photolysis of O_3 to form $O(^3P)$ is smaller in magnitude and exhibits less vertical variability than is observed for the other reactions considered. For each reaction analyzed, the El Monte aerosol causes a slight decrease in photolysis rates in the lowest 100 m, with a more pronounced enhancement observed above this height. The presence of a cross-over point at which the fractional change of a given photolysis rate is zero results from an offset between increased diffuse actinic flux due to

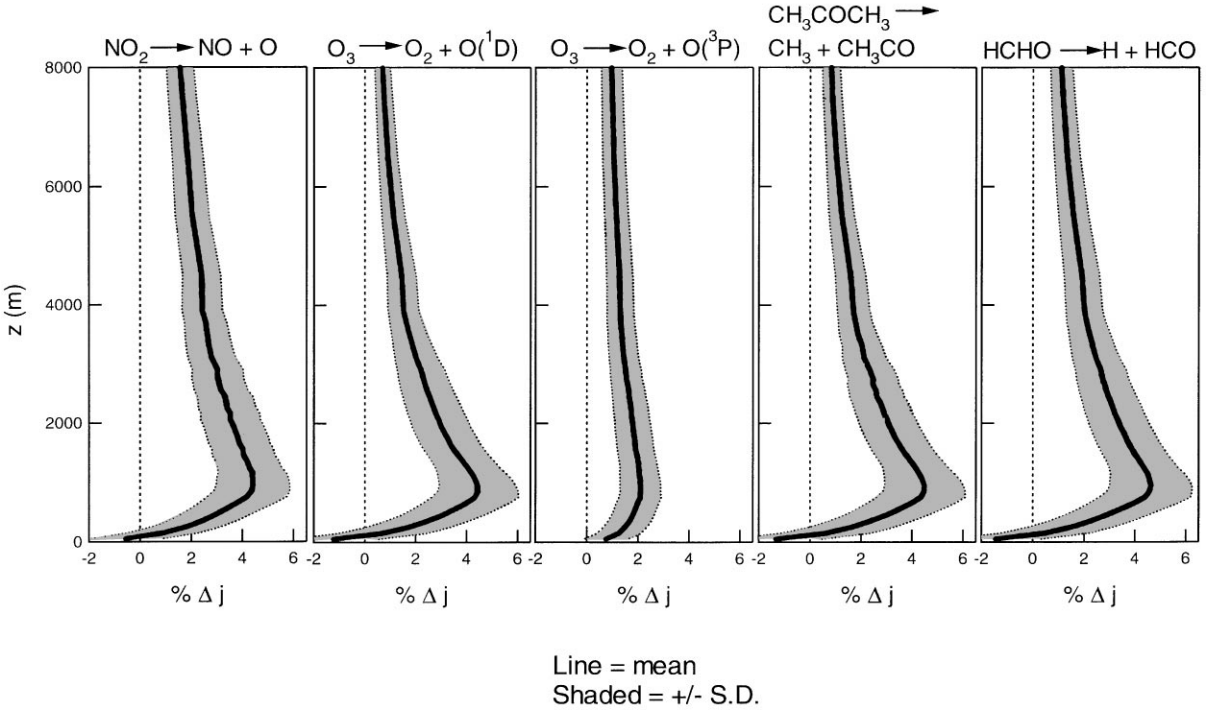

Fig. 11. Fractional change in five gas-phase photolysis rates calculated to have resulted from the aerosol sampled over El Monte relative to an aerosol-free atmosphere. For each reaction considered, the mean and standard deviation were determined from photolysis rate calculations using measurements made during spirals flown over El Monte on 10 flights. Unlike most of the other analyses presented here, altitude is relative to ground level and not sea level.

aerosol-enhanced scattering and decreased direct actinic flux caused by upward scattering and absorption by the overlying aerosol. These cross-overs have been observed in similar analyses with relatively non-absorbing aerosol like that encountered during SCOS (e.g., Liao et al., 1999). The maximum increase in photolysis rates above that expected if no aerosol were present is approximately 2% for $O_3 \rightarrow O(^3P)$, and 5% for each of the other reactions considered. Inclusion of the 2500 m aerosol layers measured during spirals over El Monte on 9 and 10 September results in a further enhancement of approximately 1% (0.3% for $O_3 \rightarrow O(^3P)$). Similar results were obtained when the fractional change in the photolysis rate of NO_2 was considered along the east–west cross section described in Fig. 4 using data from morning and afternoon flights on 28 August. As shown in Fig. 12, only slight variations in photolysis rate alteration are observed along the cross section, both in the morning and afternoon. The sharp gradient in fractional photolysis rate change with height in the lowest 500 m demonstrates the potential error caused by extrapolations of ground-based radiative flux measurements. The impact of aerosols on photolysis rates presented here is similar to estimates of Jacobson (1998) using data obtained over Long Beach on 27 August 1987 during SCAQS, but differs significantly from calculations performed using data obtained over Claremont on the same day. Specifically, Jacobson (1998) predicted that the aerosol present over Claremont resulted in a decrease of up to about 12% in the NO_2 photolysis rate, resulting from a more concentrated and highly absorbing aerosol than was sampled during SCOS. The atypical meteorological conditions

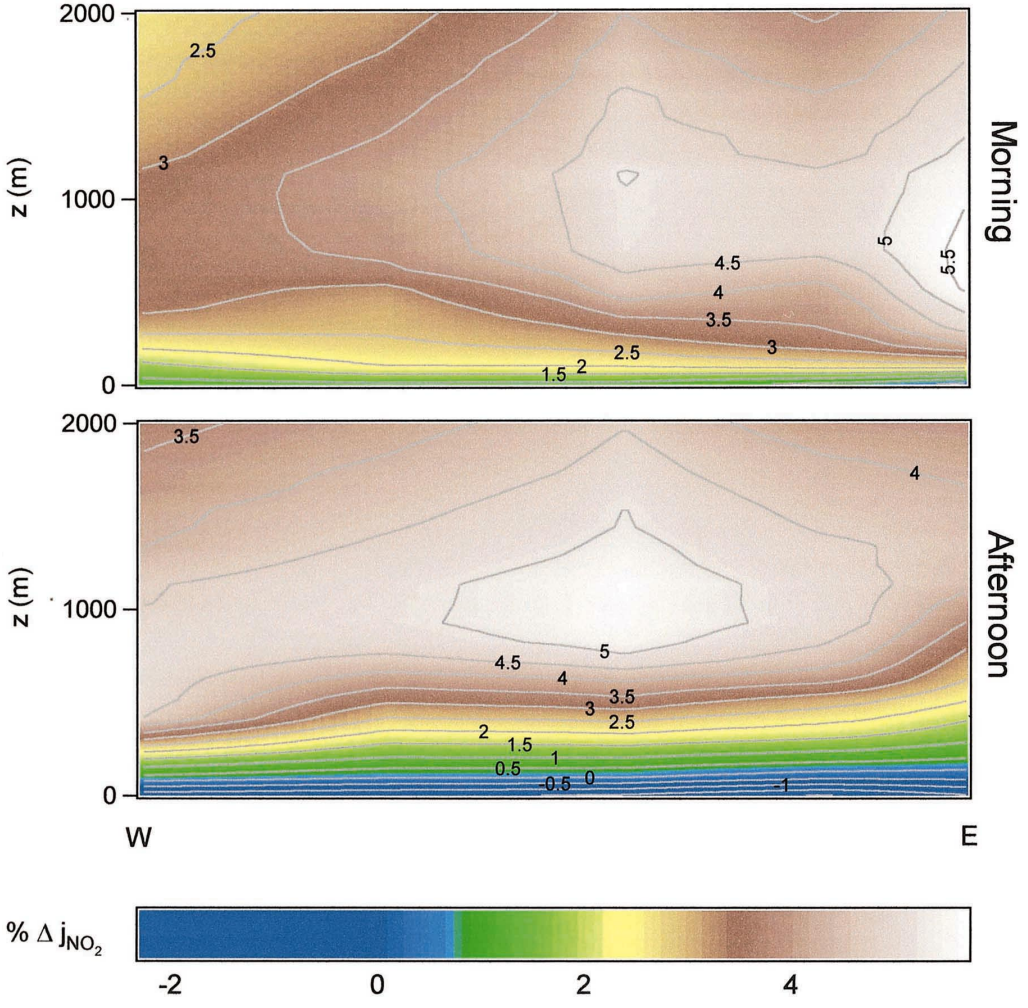

Fig. 12. Vertically resolved fractional change in the NO_2 photolysis rate calculated using data obtained during spirals flown on the morning and afternoon flights of 28 August. The east–west cross section indicated in Fig. 4 was used for presentation of these data.

during this campaign prevented a comparable severe pollution episode, while improved air quality in Southern California since 1987 would probably limit the likelihood of aerosol loadings similar to those observed in Claremont during SCAQS. Therefore, the results from SCOS and SCAQS probably bound the likely impact that a significant, present-day, pollution episode would have on photolysis rates.

6. Summary

As part of the Southern California Ozone Study (SCOS), 12 missions were conducted with an aircraft instrumented to characterize the chemical and physical properties of the Los Angeles aerosol. Instrumentation on board included three parallel filter sampling systems, three nephelometers, an absorption photometer, a DMA, and two OPCs. Data from the variety of measurements made were combined to provide a time-resolved physicochemical description of the aerosol. Several closure comparisons were performed between derived and directly measured properties. Best-fit lines through scatter plots containing these data for comparisons of fine aerosol mass, "dry" aerosol scattering coefficient, "wet" aerosol scattering coefficient, hemispherical backscattering coefficient, and absorption coefficient had derived/measured slopes of 0.91, 1.06, 1.13, 1.21, and 0.55, respectively. The exact cause of the large disagreement in the absorption comparison is not known, although a number of potential errors have been suggested.

The aerosol present over the Los Angeles Basin exhibits a complex three-dimensional structure. Vertically resolved data suggest that pronounced elevated layers present over the inland areas were formed by injection of aerosol above the ground-level polluted layer along the Southern edge of the San Gabriel Mountains, followed by advection towards the coast through incorporation into the sea breeze return flow. Additional layers were observed about 500 m asl off the coast of Santa Monica, and approximately 2500 m asl over El Monte and Long Beach. Data from spirals flown over El Monte, Fullerton, and Riverside on several flights over the 3-week sampling period were used to provide a limited statistical description of the vertically resolved aerosol at each location. In general, it was found that variability over time exceeded variability among locations. Constant altitude circles flown over Diamond Bar, Mira Loma, and Riverside yielded evidence of gradients in aerosol concentration sufficient to cause over 50% variability within a 5×5 km computational grid cell commonly used in atmospheric models.

Data from spirals flown over El Monte during several flights, as well as from spirals flown over several locations on 28 August, were used to analyze the impact of the aerosol on important photolysis rates in the photochemical generation of ozone. On average, the aerosol was predicted to cause a slight decrease in photolysis rates in the first 100 m above ground level, but led to a more pronounced (up to $\sim 5\%$) increase above that height. For most of the reactions considered, the 2500 m elevated aerosol layers above El Monte caused an enhancement in photolysis rates of about 1% above that resulting from the aerosol present below these layers. Collectively, the data obtained in this sampling program provide further insight into microphysical processes that govern the size, composition, and spatial and temporal behavior of the Los Angeles aerosol.

Acknowledgements

The authors gratefully acknowledge Prakash Bhave and Glen Cass for providing back trajectories used in this analysis. We also thank Yanzeng Zhao for assistance related to the El Monte lidar measurements. This work was supported by the California Air Resources Board.

References

Anderson, T.L., Covert, D.S., Marshall, S.F., Laucks, M.L., Charlson, R.J., Waggoner, A.P., Ogren, J.A., Caldow, R., Holm, R.L., Quant, F.R., Sem, G.J., Wiedensohler, A., Ahlquist, N.A., Bates, T.S., 1996. Performance characteristics of a high-sensitivity, three-wavelength, total scatter/backscatter nephelometer. Journal of Atmospheric and Oceanic Technology 13 (5), 967–986.

Bergstrom, R.W., 1972. Predictions of the spectral absorption and extinction cofficients of an urban air pollution model. Atmospheric Environment 6, 247–258.

Blumenthal, D.L., White, W.H., Smith, T.B., 1978. Anatomy of a Los Angeles smog episode: pollutant transport in the daytime sea breeze regime. Atmospheric Environment 12, 893–907.

Bond, T.C., Anderson, T.L., Campbell, D., 1999. Calibration and intercomparison of filter-based measurements of visible light absorption by aerosols. Aerosol Science and Technology 30 (6), 582–600.

Castro, T., Ruizsuarez, L.G., Ruizsuarez, J.C., Molina, M.J., Montero, M., 1997. Sensitivity analysis of a UV radiation transfer model and experimental photolysis rates of NO_2 in the atmosphere of Mexico City. Atmospheric Environment 31 (4), 609–620.

Chow, J.C., Watson, J.G., Fujita, E.M., Lu, Z.Q., Lawson, D.R., Ashbaugh, L.L., 1994. Temporal and spatial variations of PM(2.5) and PM(10) aerosol in the Southern California air-quality study. Atmospheric Environment 28 (12), 2061–2080.

Chow, J.C., Watson, J.G., Pritchett, L.C., Pierson, W.R., Frazier, C.A., Purcell, R.G., 1993. The dri thermal optical reflectance carbon analysis system – description, evaluation and applications in United States air-quality studies. Atmospheric Environment Part A – General Topics 27 (8), 1185–1201.

Demerjian, K.L., Schere, K.L., Peterson, J.T., 1980. Theoretical estimates of actinic (spherically integrated) flux and photolytic rate constants of atmospheric species in the lower troposphere. Advances in Environmental Science and Technology 10, 369–459.

Dickerson, R.R., Kondragunta, S., Stenchikov, G., Civerolo, K.L., Doddridge, B.G., Holben, B.N., 1997. The impact of aerosols on solar ultraviolet radiation and photochemical smog. Science 278 (5339), 827–830.

Fuller, K.A., Malm, W.C., Kreidenweis, S.M., 1999. Effects of mixing on extinction by carbonaceous particles. Journal of Geophysical Research – Atmospheres 104 (D13), 15941–15954.

Harley, R.A., Russell, A.G., Mcrae, G.J., Cass, G.R., Seinfeld, J.H., 1993. Photochemical modeling of the Southern California air-quality study. Environmental Science and Technology 27 (2), 378–388.

Hoff, R.M., Harwood, M., Sheppard, A., Froude, F., Martin, J.B., Strapp, W., 1997. Use of airborne lidar to determine aerosol sources and movement in the Lower Fraser Valley (Lfv). Bc. Atmospheric Environment 31 (14), 2123–2134.

Jacobson, M.Z., 1997. Development and application of a new air pollution modeling system. 3. Aerosol-phase simulations. Atmospheric Environment 31 (4), 587–608.

Jacobson, M.Z., 1998. Studying the effects of aerosols on vertical photolysis rate coefficient and temperature profiles over an urban airshed. Journal of Geophysical Research – Atmospheres 103 (D9), 10593–10604.

Kasten, F., 1969. Visibility in the phase of pre-condensation. Tellus 21, 631–635.

Lalas, D.P., Asimakopoulos, D.N., Deligiorgi, D.G., Helmis, C.G., 1983. Sea-breeze circulation and photochemical pollution in Athens, Greece. Atmospheric Environment 17, 1621–1632.

Lantz, K.O., Shetter, R.E., Cantrell, C.A., Flocke, S.J., Calvert, J.G., Madronich, S., 1996. Theoretical, actinometric, and radiometric determinations of the photolysis rate coefficient of NO_2 during the Mauna Loa Observatory Photochemistry Experiment 2. Journal of Geophysical Research – Atmospheres 101 (D9), 14613–14629.

Larson, S.M., Cass, G.R., Hussey, K.J., Luce, F., 1988. Verification of image-processing based visibility models. Environmental Science and Technology 22 (6), 629–637.

Li, S.M., Macdonald, A.M., Strapp, J.W., Lee, Y.N., Zhou, X.L., 1997. Chemical and physical characterizations of atmospheric aerosols over Southern California. Journal of Geophysical Research – Atmospheres 102 (D17), 21341–21353.

Liao, H., Yung, Y.L., Seinfeld, J.H., 1999. Effects of aerosols on tropospheric photolysis rates in clear and cloudy atmospheres. Journal of Geophysical Research – Atmospheres 104 (D19), 23697–23707.

Lu, R., Turco, R.P., 1994. Air pollutant transport in a coastal environment. 1. 2-Dimensional simulations of sea-breeze and mountain effects. Journal of the Atmospheric Sciences 51 (15), 2285–2308.

Lu, R., Turco, R.P., 1995. Air pollutant transport in a coastal environment. 2. 3-Dimensional simulations over Los-Angeles Basin. Atmospheric Environment 29 (13), 1499–1518.

Lu, R., Turco, R.P., Jacobson, M.Z., 1997. An integrated air pollution modeling system for urban and regional scales. 1. Structure and performance. Journal of Geophysical Research – Atmospheres 102 (D5), 6063–6079.

Lurmann, F.W., Wexler, A.S., Pandis, S.N., Musarra, S., Kumar, N., Seinfeld, J.H., 1997. Modelling urban and regional aerosols. 2. Application to California's South coast air basin. Atmospheric Environment 31 (17), 2695–2715.

Malicet, J., Daumont, D., Charbonnier, J., Parisse, C., Chakir, A., Brion, J., 1995. Ozone UV spectroscopy. 2. Absorption cross-sections and temperature-dependence. Journal of Atmospheric Chemistry 21 (3), 263–273.

McNair, L.A., Harley, R.A., Russell, A.G., 1996. Spatial inhomogeneity in pollutant concentrations, and their implications for air quality model evaluation. Atmospheric Environment 30 (24), 4291–4301.

McPeters, R., 1993, Ozone profile comparisons. In: Remsberg, E.E., Prather, M.J. (eds.), The atmospheric Effects of Stratospheric Aircraft: Report of the Models and Measurements Workshop, NASA Ref. Publ. 1292, A1–A47.

Meng, Z., Dabdub, D., Seinfeld, J.H., 1997. Chemical coupling between atmospheric ozone and particulate matter. Science 277 (5322), 116–119.

Meng, Z.Y., Dabdub, D., Seinfeld, J.H., 1998. Size-resolved and chemically resolved model of atmospheric aerosol dynamics. Journal of Geophysical Research – Atmospheres 103 (D3), 3419–3435.

Moelwyn-Hughes, E.A., 1961. Physical Chemistry. Pergamon, Tarrytown, NY.

Nagatani, R.M., Rosenfield, J.E., 1993. Temperature, heating, and circulation. In: Remsberg, E.E., Prather, M.J. (eds.), The Atmospheric Effects of Stratospheric Aircraft: Report of the Models and Measurements Workshop, NASA Ref. Publ. 1292, A1–A47.

Neckel, H., Labs, D., 1984. The solar-radiation between 3300-a and 12500-a. Solar Physics 90 (2), 205–258.

Pandis, S.N., Harley, R.A., Cass, G.R., Seinfeld, J.H., 1992. Secondary organic aerosol formation and transport. Atmospheric Environment Part A – General Topics 26 (13), 2269–2282.

Pandis, S.N., Wexler, A.S., Seinfeld, J.H., 1993. Secondary organic aerosol formation and transport. 2. Predicting the ambient secondary organic aerosol-size distribution. Atmospheric Environment Part A – General Topics 27 (15), 2403–2416.

Patterson, E.M., Gillette, D.A., Stockton, B.H., 1977. Complex index of refraction between 300 and 700 nm for Saharan aerosols. Journal of Geophysical Research 82, 3153–3160.

Ruggaber, A., Dlugi, R., Nakajima, T., 1994. Modeling radiation quantities and photolysis frequencies in the troposphere. Journal of Atmospheric Chemistry 18 (2), 171–210.

Saxena, P., Hildemann, L.M., McMurry, P.H., Seinfeld, J.H., 1995. Organics alter hygroscopic behavior of atmospheric particles. Journal of Geophysical Research – Atmospheres 100 (D9), 18755–18770.

Seinfeld, J.H., Pandis, S.N., 1998. Atmospheric Chemistry and Physics. Wiley–Interscience, New York.

Stamnes, K., Tsay, S.C., Wiscombe, W., Jayaweera, K., 1988. Numerically stable algorithm for discrete-ordinate-method radiative-transfer in multiple-scattering and emitting layered media. Applied Optics 27 (12), 2502–2509.

Tang, I.N., 1996. Chemical and size effects of hygroscopic aerosols on light scattering coefficients. Journal of Geophysical Research – Atmospheres 101 (D14), 19245–19250.

Tang, I.N., Munkelwitz, H.R., 1994. Water activities, densities, and refractive-indexes of aqueous sulfates and sodium-nitrate droplets of atmospheric importance. Journal of Geophysical Research – Atmospheres 99 (D9), 18801–18808.

Tang, I.N., Tridico, A.C., Fung, K.H., 1997. Thermodynamic and optical properties of sea salt aerosols. Journal of Geophysical Research – Atmospheres 102 (D19), 23269–23275.

Tegen, I., Fung, I., 1994. Modeling of mineral dust in the atmosphere – sources, transport, and optical-thickness. Journal of Geophysical Research – Atmospheres 99 (D11), 22897–22914.

Wakamatsu, S., Ogawa, Y., Murano, K., Goi, K., Aburamoto, Y., 1983. Aircraft survey of the secondary photochemical pollutants covering the Tokyo Metropolitan Area. Atmospheric Environment 17, 827–835.

Wakimoto, R.M., McElroy, J.L., 1986. Lidar observation of elevated pollution layers over Los-Angeles. Journal of Climate and Applied Meteorology 25 (11), 1583–1599.

White, W.H., 1990. Rep. No. 24, Natl. Acid Precip. Assess. Program, Washington, DC.

Woods, T.N., Prinz, D.K., Rottman, G.J., London, J., Crone, P.C., Cebula, R.P., Hilsenrath, E., Brueckner, G.E., Andrews, M.D., White, O.R., Van Hoosier, M.E., Floyd, L.E., Herring, L.C., Knapp, B.G., Pankratz, C.K., Reiser, P.A., 1996. Validation of the VARS Solar irradiances: Comparison with the ATLAS 1 and 2 measurements. Journal of Geophysical Research – Atmospheres 101 (D6), 9541–9569.

World Meteorological Organization (WMO), 1985. Rep. No. 16.

Zhang, X.Q., McMurry, P.H., Hering, S.V., Casuccio, G.S., 1993. Mixing characteristics and water content of submicron aerosols measured in Los Angeles and at the Grand Canyon. Atmospheric Environment 27, 1593–1607.